

# Amorphous silicon structures generated using a moment tensor potential and the activation relaxation technique *nouveau*

Karim Zongo<sup>1,\*</sup>, Hao Sun<sup>2</sup>, Claudiane Ouellet-Plamondon<sup>1</sup>, Normand Mousseau<sup>3</sup>, and Laurent Karim Béland<sup>2,\*</sup>

<sup>1</sup>Département de génie de la construction, École de Technologie Supérieure, Université du Québec, Montréal, QC, Canada

<sup>2</sup>Department of Mechanical and Materials Engineering, Queen's university, Kingston, ON, Canada

<sup>3</sup>Département de physique, Institut Courtois and Regroupement québécois sur les matériaux de pointe, Université de Montréal, Montréal, QC, Canada

Correspondence: Karim Zongo (karim.zongo.2@ens.etsmtl.ca) or Laurent Karim Béland (laurent.beland@queensu.ca)

## Abstract

Preparing realistic atom-scale models of amorphous silicon (a-Si) is a decades-old condensed matter physics challenge. Herein, we combine the Activation Relaxation Technique *nouveau* (ARTn) to a Moment Tensor Potential (MTP) to generate seven a-Si models containing between 216 and 4096 atoms. A thorough analysis of their short-range and medium-range structural properties is performed, alongside assessments of excess energy and mechanical properties. The seven ARTn-MTP models are compared with available experimental data and other high quality a-Si models present in the literature. The seven ARTn-MTP a-Si models are in excellent agreement with available experimental data. Notably, several of our models, including the 216-atom, 512-atom, and 1000-atom a-Si models, exhibit low coordination defects without any traces of crystalline grains. Historically overlooked in previous research, our study underlines the need to assess the validity of the continuous random-network hypothesis for the description of *perfect* amorphous model by characterizing local crystalline environment and to explore the crystallisation process of a-Si through modelling.

## I. Introduction

Amorphous silicon (a-Si) is used in applications that include photovoltaics, thin-film transistors, battery electrodes, and liquid-crystal displays<sup>1–5</sup>. Recent advances include its use as coating materials for next-generation gravitational wave detectors<sup>6</sup>. Additionally, a-Si serves as the canonical disordered solid prototype for the development of modeling methods.

a-Si<sup>7,8</sup> is idealized as a continuous random network (CRN)<sup>9</sup>, characterized by a local atomic environment akin to crystalline silicon<sup>10,11</sup>. It maintains a local tetrahedral crystalline environment without long-range order. Real a-Si, however, is believed to contain defects associated with its disordered nature at a level that depends on its preparation<sup>6,12–15</sup>. These include local coordination defects, medium-range ring defects and two-level systems—the latter contribute to noise in sensitive gravitational wave detectors and cause decoherence in quantum computers<sup>6,15</sup>. Variations in tetrahedral geometry and bond lengths also significantly affect a-Si's performance. Controlling structural anomalies during preparation poses challenges from both an experimental and a theoretical perspective. Indeed, the structure of a-Si is highly influenced by preparation methods<sup>16</sup>; for instance, chemical vapor deposition<sup>17</sup> and ion implantation<sup>13,18,19</sup> can introduce voids and coordination defects. Thermal annealing<sup>13,18,20,21</sup> often refines these imperfections, enhancing material quality.

Extensive theoretical research has focused on developing realistic structural models for a-Si<sup>10,22–27</sup>. Various methods for simulating materials, including a-Si, can be

categorized into dynamic and non-dynamic approaches<sup>7,8</sup>. Dynamic methods, traditionally based on density functional theory (DFT)<sup>28</sup> or semiempirical force fields<sup>29</sup>, primarily use melt-quench processes. However, these methods face challenges: experimental a-Si cannot be produced by melt-and-quench, DFT simulations are limited in system size and quenching rate, and semi-empirical force fields are often compromised by limited accuracy and transferability issues.

Non-dynamic methods include the Reverse Monte Carlo (RMC) approach<sup>30–34</sup>. In RMC, the computer-generated a-Si structure is randomly modified in order for its simulated structure factor and radial distribution function  $g(r)$  to match experimental data. RMC's main drawback is that it can yield multiple configurations for the same  $g(r)$  — in other word the solution is degenerate. To overcome this, hybrid RMC methods incorporate force field interactions, ensuring generated configurations are both consistent with experimental data and physically realistic. Variants like the force-enhanced atomic refinement<sup>35,36</sup> and experimentally constrained molecular relaxation<sup>37</sup> utilize semi-empirical and DFT interactions, respectively. Other key non-dynamic methods include the Wooten-Winer-Weaire (WWW) bond-switching algorithm<sup>10</sup>, which optimizes atomic configurations by minimizing energy, and the Activation-Relaxation Technique *nouveau* (ARTn)<sup>22,38–40</sup>, which combines activation and relaxation steps to discover low-energy structures. ARTn can be paired with various force fields and *ab initio* methods, making it suitable for applications that include relaxation of disordered systems and diffusion processes<sup>15,41–49</sup>.

One of the key components in both dynamical and

non-dynamical methods is the interaction potential. The ongoing challenge of balancing accuracy and computational cost in these methods has led to the development of machine learning interatomic potentials (MLIPs)<sup>50–52</sup>. MLIPs combine descriptors of the atomic environment, regression methods, and DFT data. Many MLIPs frameworks have been developed, including artificial neural networks<sup>50,53</sup>, kernel-based methods<sup>54,55</sup>, and linear regression approaches<sup>56,57</sup>, among others. For a detailed description of MLIPs, including their implementation and testing, the reader is referred to the existing literature<sup>52</sup>. In the case of a-Si, structures have been modeled using artificial neural networks<sup>58–60</sup> and Gaussian Approximation Potentials (GAP)<sup>54,55</sup>. In initial studies, the GAP potential was applied to a-Si systems containing between 512 and 4,096 atoms<sup>24</sup>. Later, the GAP model was extended to larger systems of up to 100,000 atoms to investigate the atomistic mechanisms underlying various structural transitions in disordered silicon<sup>61</sup>. Other MLIPs, such as the Moment Tensor Potential<sup>57</sup> (MTP), have also been applied to a-Si<sup>62</sup>. In these studies, melt-quench MD simulations were employed to generate a-Si structures.

A natural next step is to couple ARTn<sup>22,38–40</sup> with machine learning potential to generate a-Si models. The objective of this paper is to generate a-Si models using ARTn-ML, which could enhance our understanding of the a-Si model and open new avenues for further research. The manuscript is organized into three main sections. The Methods section outlines the principles of the ARTn method and details our input models, the ARTn-MTP simulation process, and the analytical tools used. The Results and Discussion Section presents findings from our analysis of the configurations generated by ARTn-MTP. Finally, the key insights and discoveries of our study are summarized in the conclusions.

## II. Methods

### A. Activation Relaxation Technique *nouveau*

ARTn<sup>22,38</sup> is a computational method used in the study of activated processes, particularly in the context of diffusion and transitions between states in condensed matter systems. ARTn is designed to simulate rare events that signify substantial changes in the microscopic structure of atomic systems, based on the efficient exploration of potential energy landscapes. ARTn employs an event-driven approach in which the system evolves by transitioning between different states or configurations. The concept is based on the understanding that within the configurational space, there is a distinct set of points representing saddle points and adjacent minima in the potential energy surface of the system. As the name implies, ARTn can be summarized as a two-step process<sup>22</sup>: activation and relaxation. In the activation step, starting from a local energy minimum, the configuration is pushed toward a nearby first-order saddle point. In the relaxation step, the system is driven over the saddle point and then relaxed to a new energy minimum. The new configuration is

accepted based on the Metropolis acceptance probability, which is given by  $P_{\text{accept}} = \min(1, \exp(-\frac{\Delta E}{kT}))$ , where  $T$  is the fictitious temperature, set to 0.25 eV for our simulation,  $k$  is the Boltzmann constant, and  $\Delta E$  is the energy difference between the old and new configurations<sup>22,23,63</sup>. The search is restricted to paths that include only saddle points. The ARTn method has demonstrated its value in revealing rare events that conventional simulation methods may struggle to capture due to the slow dynamics and relaxation inherent in these systems. Detailed descriptions of the method can be found elsewhere<sup>22,38,39,64,65</sup>.

### B. A moment tensor potential for silicon

In practical terms, ARTn serves as a saddle-point search engine, employing an interaction potential as both a force and energy calculator. The simulation's accuracy is directly influenced by the selection of the force field. Previous studies have relied on semi-empirical force field<sup>15,22,42,66,67</sup> and ab initio methods<sup>44,68,69</sup>. Here we employ a machine learning-based forcefield. This potential was developed to jointly describe Si, O, and SiO<sub>2</sub> systems<sup>62</sup>, and is an improvement over a previously reported Si MTP<sup>70</sup>. This potential is based on the MTP framework<sup>57,71</sup>. A detailed description of the development and implementation of this MTP can be found in our previous work<sup>62,70</sup>.

### C. Protocol for input models preparation and simulation details

We prepared models containing 216, 512, 1000, and 4096 atoms. For the model with 216 atoms, we used two different simulation boxes corresponding to densities of 2.20 g/cm<sup>3</sup> (216-R1) and 2.28 g/cm<sup>3</sup> (216-R2), respectively. These two boxes were randomly filled with an overlap distance (initial atomic separation) of 2.3 Å for 2.20 g/cm<sup>3</sup> and 2 Å for 2.28 g/cm<sup>3</sup>. For the 512-atom model, we employed two simulation boxes randomly filled with atoms, using the same densities as those applied to the 216-atom model. The first 512-atom model had a density of 2.20 g/cm<sup>3</sup> (512-R1) with an initial overlap of 2.3 Å. The second 512-atom model (512-R2) along with the 1000-atom model (1000-R) were randomly filled with a density of 2.28 g/cm<sup>3</sup> and an initial overlap of 2 Å. The search for events during ARTn-MTP simulations was initiated using configurations that were already at local minima. Herein, the ARTn simulations begins by applying random displacements to the chosen central atom and its neighbors, based on a user-defined local cut-off radius. Once the displacements are introduced, the algorithm searches for convergence to a saddle point, guided by the lowest curvature. After locating the saddle point, the minimization process begins to find the new minimum. The minimization is carried out using either the Steepest Descent (SD) or the Fast Inertial Relaxation Engine (FIRE) algorithm. In all ARTn-MTP simulations, we used a fictitious temperature of 0.25 eV in the Metropolis accept-reject criterion. Each simulation started with

Models name	Input configurations for a-Si preparation	N atoms	a-Si preparation methods
216-R1	Randomly filled	216	ARTn runs using MTP potential
216-R2	Randomly filled	216	ARTn runs using MTP potential
216-FEAR	Randomly filled	216	Force hence atomic refinement <sup>36</sup>
512-R1	Randomly filled	512	ARTn runs using MTP potential
512-R2	Randomly filled	512	ARTn runs using MTP potential
512-MD	Randomly filled	512	MD simulation using MTP potential
512-RMC	Randomly filled	512	Reverse monte carlo simulation <sup>24,72</sup>
512-INV	Randomly filled	512	Invariant environment refinement technique <sup>24,72</sup>
512-FEAR	Randomly filled	512	Force hence atomic refinement <sup>36</sup>
512-WWW	Randomly filled	512	Bond switching algorithm <sup>24,72</sup>
1000-R	Randomly filled	1000	ARTn runs using MTP potential
4096-R-MD	Randomly filled + MD runs	4096	ARTn runs using MTP potential
4096-WWW	Randomly filled	4096	Bond switching algorithm <sup>36</sup>
100k-GAP18	Unknown	100000	MD simulation using GAP potential <sup>61</sup>
1000-aSi-SW	Amorphous configuration <sup>22,38,68</sup>	1000	ARTn runs using MTP potential

**Tab. I** A summary of the models discussed in this study. The preparation methods for the input configurations, the number of atoms in each model, and the preparation methods for the final a-Si models are provided. Models without a reference were prepared for this work following the protocol discussed in the methods section.

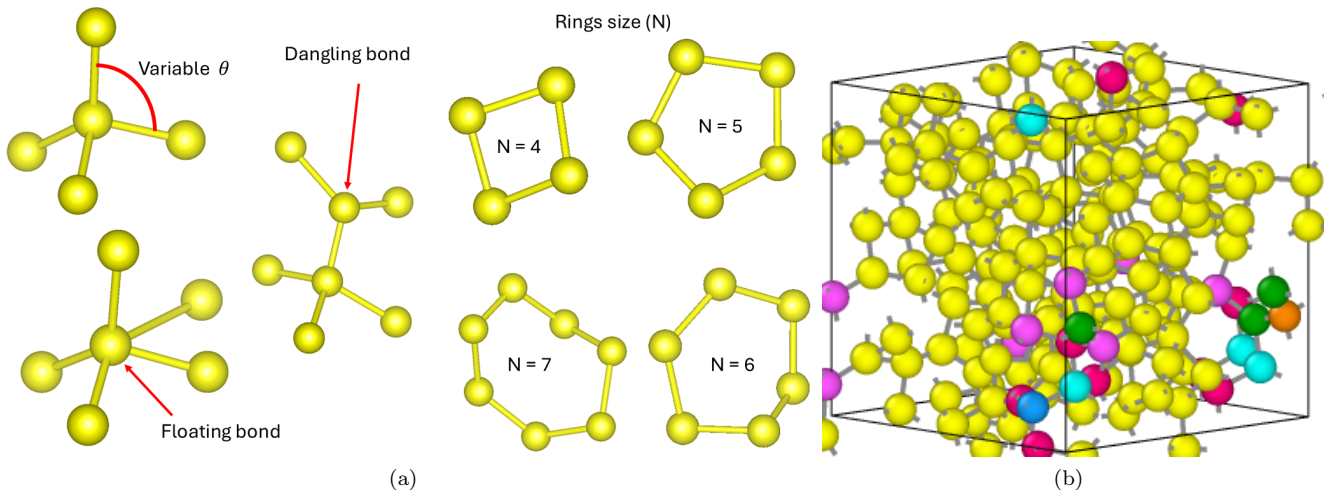


**Fig. 1** Key structural elements characterizing a-Si: (a) bond angle ( $\theta$ ), coordination defects such as dangling bonds (3-fold bonded atoms) and floating bonds (5-fold bonded atoms), and ring structures, including 4-, 5-, 6-, and 7-membered rings. (b) A 100% 4-fold fully coordinated amorphous structure comprising 216 atoms, generated by ARTn-MTP simulation, with 14.40 atoms in a crystalline environment. The atoms shown in yellow within the box are in an amorphous environment, while those colored differently are in a crystalline environment, specifically cubic or hexagonal diamond.

event searches initiated with a local cut-off radius of 3 Å, which the algorithm used to identify the region around the selected central atom which will be deformed. This cut-off radius was progressively increased to a maximum cut-off 5.5 Å in order to expand the local zone of initial deformation when the ARTn moves no longer led to energy decrease. The coordination defects level was monitored during the simulations. For coordination defect levels above 5 %, the full list of atoms was used as potential central atoms for ARTn moves. For defect levels at or below 5 %, only atoms with a non-four-fold coordination were allowed to serve as the central atom in ARTn moves.

#### D. Structural analysis

We employ a set of criteria to assess the quality of our amorphous structures. These criteria are derived from considerations of short-range structures, coordination defects, and intermediate-range order. Understanding these different structural aspects is crucial in the study of materials properties, as they influence the physical, chemical, and mechanical behavior of materials. We conduct coordination analysis using OVITO<sup>73</sup> with a bond-length cutoff of 2.85 Å. The analysis of the ring size distribution, providing insights into intermediate-range order, is performed using the R.I.N.G.S code<sup>74</sup> based on the King criteria. We employed the ISAACS code<sup>75</sup> for the calculation of the structure factor while the radial distribution function

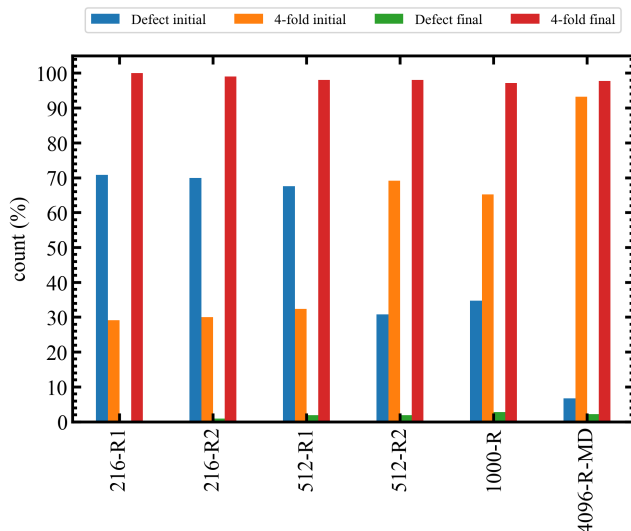


**Fig. 2** Coordination numbers of input configurations and ARTn-MTP optimized configurations (final configurations). All non-4-fold coordinated atoms, including under- and over-coordinated atoms, are considered defective. The models analyzed include 216, 512, 1000 and 4096 atoms.

and angular distribution function were determined using LAMMPS<sup>76</sup> through pseudo simulations.

We also measure the amount of crystallinity in the models. Here, crystallinity refers to environments that are cubic or hexagonal diamond to second neighbour, all atoms at the center of this environment or within the first- and second-neighbour shell of a perfectly atom are considered as having crystallinity. We use method developed by Ref.<sup>77</sup> as implemented in OVITO<sup>73</sup>.

### III. Results and discussion

Models of size 216 atoms, 512 atoms, 1000 atoms and 4096 atoms were generated as detailed in table I. We analyze these configurations with respect to short-range order, medium-range order, electronic properties as well as mechanical properties. Fig. 2 displays the defects in both the input and final configurations. The input configurations exhibit a higher prevalence of coordination defects than the final configurations: approximately 70% for the 216-R1, 216-R2, and 512-R1 models, compared to around 30% for the 512-R2 and 1000-R models, as illustrated by the blue bars. The green bars represent the total number of defects present in the final configurations.

In all ARTn-MTP a-Si models, the final percentage of defective atoms remained below 2%, with the exception of the 1000-R and 4096-R-MD models, which exhibit a final defect percentage of approximately 3%. The initial 4-fold coordination number (shown by the orange bars in Fig. 2) is approximately 30% for the 216-R1, 216-R2, and 512-R1 models, and around 68% for the 512-R2 and 1000-R models. In contrast, the final configurations display markedly higher 4-fold coordination numbers (depicted

by the red bars in Fig. 2 and Table II), with values of 99.07%, 100%, 98.04%, 98.04%, 97.20%, and 97.80% for the 216-R1, 216-R2, 512-R1, 512-R2, 1000-R and 4096-R-MD models, respectively. No atoms with fewer than 3 neighbors or more than 5 neighbors were observed.

To further contextualize the number of coordination defects in the ARTn-MTP a-Si models, we present a comparison in Fig. 5, which includes data from the literature as well. First, all the models presented show no atoms with fewer than 3 neighbors or more than 5 neighbors. Secondly, all of the ARTn-MTP generated models exhibit fewer floating and dangling bonds compared to all other methods, except the WWW model and 100k-GAP18 model. Notably, the 216-R2 model is absent from Fig. 5 because it contains 100% four-fold coordination. To our knowledge, no other a-Si models exhibit 100% four-fold coordination, except for some WWW models generated with a Keating-type potential<sup>23,78</sup>

The last column of Table II presents the fraction of atoms in a crystalline environment (cubic or hexagonal diamond). As shown, most of the generated a-Si models, particularly those from MD simulations, contain some proportion of crystallinity. Although WWW is known to produce large a-Si models without coordination defects, the WWW a-Si models still exhibit traces of crystallinity. We identified four models—216-R1, 512-R1, 512-R2, and 1000-R—that are free from crystallinity. Furthermore, as indicated in Table III, both the 1000-aSi-SW initial and 1000-aSi-SW final configurations also contain no crystallinity. It is important to note that all four of our a-Si models without crystallinity, including the 1000-aSi-SW initial model, were generated starting from a random state without any prior MD prerun, meaning their boxes were initially filled randomly. From Table II, we note three potential trends. (i) this fraction does not seem to depend much on the system size. (ii) Starting ARTn from a random state seems to lead to a less crystalline state than starting from a melt-and-quench state. (iii) Fewer coordination defects seem to favor a higher crystallinity content. Now that, with reliable ML potentials, we can generate similar quality models using different pathways (non-dynamic melt-and-quench methods), we can start examining the link between local crystallinity, defects and the ideal continuous-random networks. This can lead to understanding why, for example, amorphous silicon cannot be produced experimentally from the liquid phase and crystallizes well below melting as well as whether the CRN model corresponds really to ideal a-Si. The ML potential<sup>62,70</sup>, which leads to high-quality models, makes further study on this question now possible.

#### A. Short-range order structural analysis of the models

Fig. 3 illustrates the structural properties of the 216-R2 models, including the angular distribution function, radial distribution function, and bond length distribution. Panels a), b), and c) display these properties for the randomly packed input configuration (216-R2), while

**Tab. II** Structural characteristics of ARTn-MTP generated amorphous models. This includes density, the positions of the first ( $r_1$ ) and second ( $r_2$ ) peaks of the RDF, average coordination number, average bond angle (with variability indicated in parentheses), and the percentages of 3-fold, 4-fold, and 5-fold coordinated atoms in each mode. A comparison is provided with previously published models. Bold fonts are used to highlight models where fewer than 3 % of atoms were mis-coordinated. Crystallinity is defined as discussed in the Methods section. Cells are left empty when information is not available for models from the literature.

Model	density	$r_1$	$r_2$	Coordination number	$\langle\theta\rangle$ ( $\sigma$ )	3-fold (%)	5-fold (%)	4-fold (%)	Crystallinity (%)
216-R1	2.20	2.36	3.77	<b>3.990</b>	109.20 (9.95)	0.93	0.00	<b>99.07</b>	0.00
216-R2	2.28	2.36	3.70	<b>4.000</b>	109.19 (10.02)	0.00	0.00	<b>100.00</b>	14.40
216-FEAR <sup>36</sup>	2.33	2.36	3.81	4.028	108.52 (15.59)	1.39	4.17	94.44	
512-R1	2.20	2.36	3.90	4.008	109.11 (11.39)	0.59	1.37	<b>98.04</b>	0.00
512-R2	2.28	2.36	3.90	4.015	108.99 (11.76)	0.19	1.76	<b>98.04</b>	0.00
512-MD	2.28	2.37	3.83	3.996	109.05 (10.95)	1.37	0.98	<b>97.65</b>	3.30
512-RMC <sup>24,72</sup>	2.30	2.34	3.66	4.039	108.57 (14.16)	1.56	5.47	92.96	3.30
512-INV <sup>24,72</sup>	2.31	2.34	3.86	4.054	108.56 (14.47)	1.95	7.42	90.62	0.00
512-WWW <sup>24,72</sup>	2.27	2.34	3.94	4.008	109.05 (10.36)	0.19	0.98	<b>98.82</b>	10.00
512-FEAR <sup>36</sup>	2.33	2.35	3.82	4.008		1.17	2.73	95.90	
512-GAP18 <sup>24</sup>	2.27	2.36	3.76	4.004	109.20 (9.60)	0.58	0.98	<b>98.44</b>	6.4
1000-R	2.28	2.37	3.76	4.020	108.94 (12.31)	0.6	2.6	97.20	0.00
4096-R-MD	2.28	2.37	3.83	4.012	109.14 (10.65)	0.51	1.44	<b>98.05</b>	6.40
4096-WWW <sup>36</sup>	2.33	2.36	3.78	4.004		0.05	0.49	<b>99.46</b>	
100k-GAP18 <sup>61</sup>	2.27	2.36	3.83	4.003	109.17 (9.99)	0.69	0.95	<b>98.35</b>	6.5

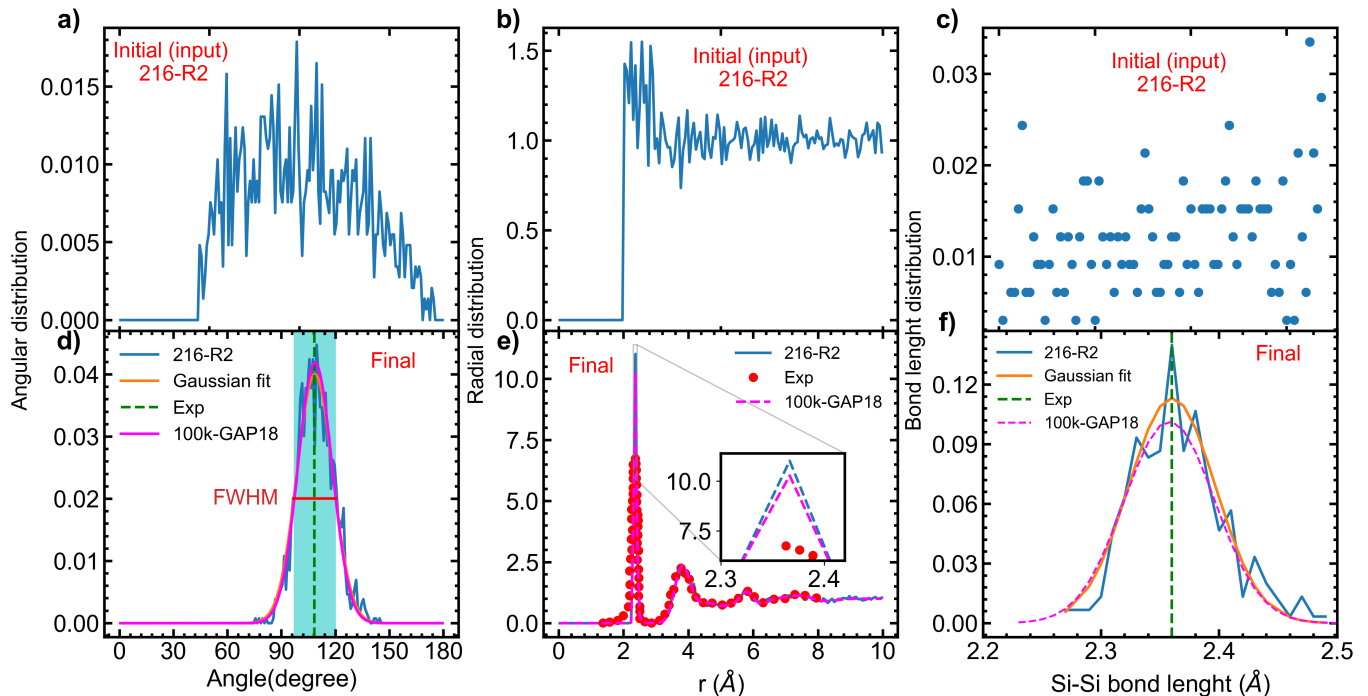


**Fig. 3** Comparison of the local structural properties of input configurations (top panels: a, b, and c) with the final configuration (100% coordinated) (bottom panels: d, e, and f) generated using the ARTn-MTP coupling scheme. The structural properties analyzed include angular distribution, radial distribution, and bond length distribution for a system comprising 216 atoms. Experimental data and data from the 100k-GAP18 model<sup>61</sup> are included to assess the quality of our 100% 4-fold coordinated 216-atom a-Si model

panels d), e), and f) show the properties of the final configurations (216-R2) produced by ARTn-MTP. The final 216-R2 configuration is 100% fully coordinated, with no coordination defects present. As shown in Fig. 3 a), b), and c), the data for the input configurations are

randomly distributed and widespread. In contrast, the data for the final configurations, depicted in Fig. 3 d), e), and f), follow well-defined distributions. The shape of the radial distribution function matches the experimental data, though the peak is somewhat overestimated. This

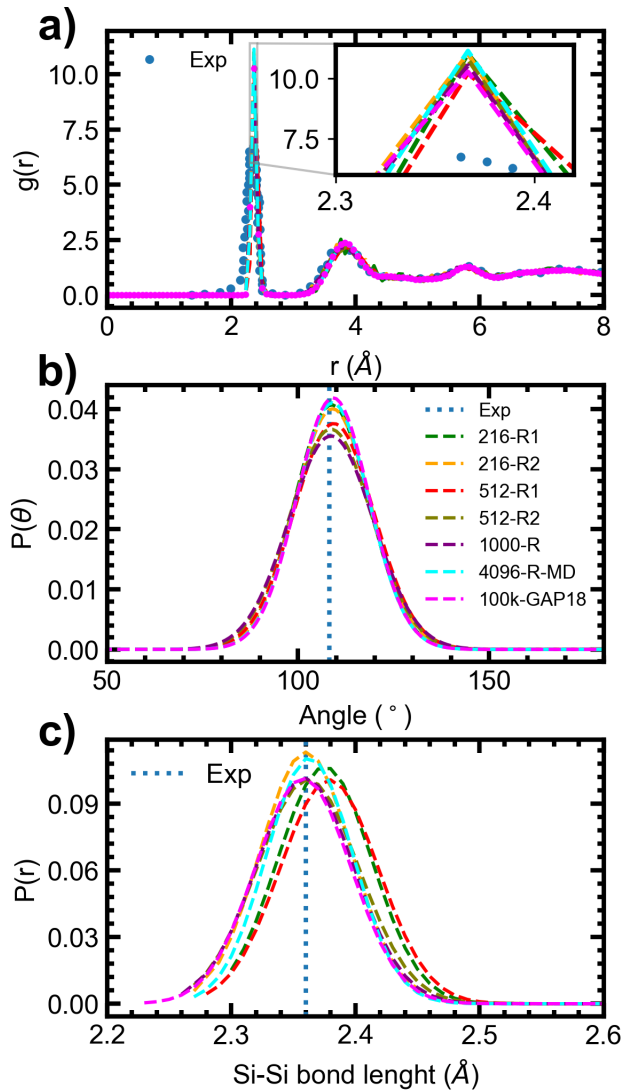


**Fig. 4** Local structural properties of ARTn-MTP generated a-Si models: (a) radial distribution, (b) angular distribution, and (c) bond length distributions. Also shown are the properties obtained from experimental data and the 100k-GAP18 atom simulations.

indicates that the Si-Si pair distances in our model are widely distributed around the experimental pair separation distance. The bond angle distribution function is centered around the tetrahedral value of  $109.5^\circ$  with a spread of  $9.96^\circ$ . A Gaussian fit to the data reveals a full width at half-maximum (FWHM) of  $23.45^\circ$ . The half width at half-maximum (HWHM) is  $11.73^\circ$ , which is similar to the experimental HWHM value of  $11^\circ$ <sup>20</sup>. For the bond length, the data for the input configuration (3 c) are widespread. In contrast, for the final configuration (3 f), the bond lengths follow a Gaussian distribution centered around the experimental value of  $2.35$  Å. The mean bond length is  $2.36$  Å, with a spread of  $0.03$  Å. The angular distribution function, radial distribution function, and bond length distribution of the final model (216-R2) were

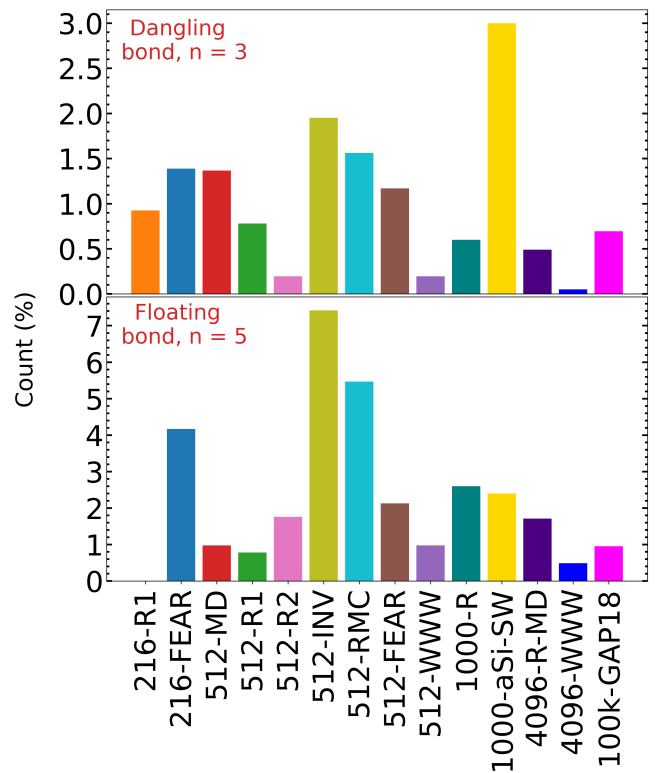


**Fig. 5** Proportion of coordination defects in various a-Si models generated by different methods. 216-R1 has no floating bond and 216-R2 is 100 % fully 4-fold coordinated. No atoms with fewer than 3 neighbors or more than 5 neighbors have been recorded in any model.

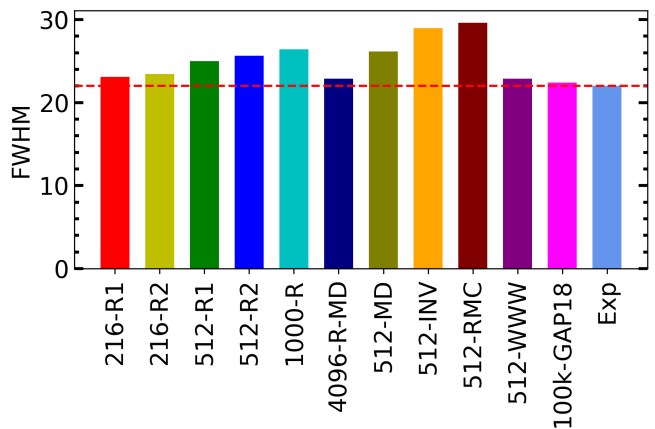


**Fig. 6** FWHM of the bond-angle distribution. The FWHM values are computed by fitting a Gaussian distribution to the bond angle distributions. The red line denotes the experimental value of FWHM<sup>20</sup>.

compared with those of the 100k-GAP18 configuration, which contains 100,000 atoms. As shown in Fig. 3 (d), (e), and (f), these properties align well with those of the larger 100k-GAP18 model. This demonstrates the high quality of our fully coordinated a-Si model. Beyond the analysis of the fully coordinated configuration, we also explore

the short-range order structure in our other models. The detailed results are presented in Fig. 4 and Tab. II. Once again, the structural properties—including the radial distribution function (Fig. 4 a), bond angle distribution function (Fig. 4 b), and bond length distribution (Fig. 4 c)—closely match experimental data and those of 100k-GAP18 models. The data for all the models presented in Fig. 4 show similar behavior, with the exception of the Si-Si bond length distribution. Notably, the bond lengths for two of our models—216-R1 (in green) and 512-R1 (in red)—are shifted. These two models have a density of  $2.20 \text{ g/cm}^3$ , which is lower than that of the other models, which is  $2.28 \text{ g/cm}^3$ . Since amorphous silicon features local tetrahedral bonding, we quantify the deviation from ideal tetrahedral geometry by calculating the FWHM for all models included in this study, as presented in Fig. 6. The FWHM values for all our models closely align with the experimental data, as well as with the WWW model and the 100k-GAP18 models.

### B. Medium-range order structural analysis of the models

We further analyze the ARTn-MTP a-Si models at intermediate length scales using the structure factor and ring statistics. Fig. 3 illustrates the static structure factor of our fully coordinated 216-R2 a-Si model, alongside experimental data and the 100k-GAP18 model. Additionally, the structure factors for the 512-R2, 1000-R, and 4096-R-MD models are included to provide a comprehensive comparison with both the experimental  $S(q)$  and the  $S(q)$  of the 100k-GAP18 models. As shown, the structure factors of all our models align well with the experimental data, with the exception of the first peak at  $S(q)$  near  $q = 2 \text{ \AA}^{-1}$ , which is underestimated by the 216-R2, 512-R2, and 1000-R models. This is consistent with other results from the literature<sup>24,36</sup> and is attributed to the system size rather than a specific method. Thus, the 4096-R-MD model, which consists of 4096 atoms, and the 100k-GAP18 model, comprising 100,000 atoms, both exhibit a strong match with the first peak of the experimental  $S(q)$ . The first peak, known as the first sharp diffraction peak, is typically underestimated in systems with fewer than a thousand atoms<sup>24,36</sup>. The height of this peak serves as a measure of structural ordering.

Ring statistics are illustrated in Fig. 8. Crystalline silicon, characterized by its diamond-type structure, primarily features 6-membered rings, while amorphous silicon tends to favor rings of sizes 5, 6, and 7. Rings with fewer than 5 members or more than 7 are typically regarded as ring defects. Notably, no 3-membered rings are observed in any of the models. Additionally, very few 4-membered rings, which are known to introduce structural stress, were recorded across all models. As shown in Fig. 8 (a-f), each model predominantly contains 5, 6, and 7-membered rings, consistent with existing literature. These ring sizes are energetically favorable for a-Si. Furthermore, all models exhibit a few larger ring defects with sizes greater than 7, as detailed in Fig. 8.

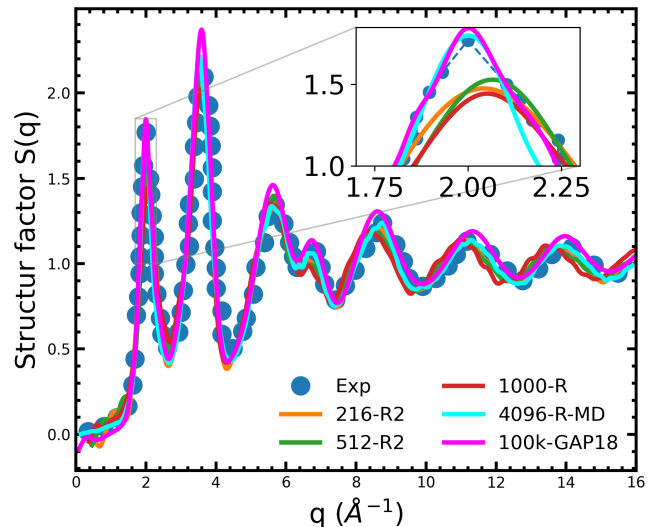


**Fig. 7** Structure factor for ARTn-MTP generated models compared with that obtained from experimental data and 100k-GAP18 atom simulations.

### C. Refinement of ART-SW optimized model: 1000-aSi-SW

As we first test the capability of ARTn coupled with MLIP to model amorphous systems, it is essential to explore several scenarios. A key consideration is the starting input configuration (see Table I). Starting from a completely random state presents a challenge, particularly for larger systems. Ideally, the process should begin from a local minimum, which can be obtained through methods such as MD runs, CG relaxation, or ARTn coupled with a semi-empirical model. In this section, we present preliminary results that demonstrate the capability of ARTn-MTP to push the limits of relaxation for a configuration already optimized by ARTn coupled with the Stillinger-Weber (SW) potential<sup>79</sup>.

A previously published a-Si model<sup>22,38</sup> using ARTn with the SW potential<sup>79</sup>, modified by Vink<sup>80</sup>, served as input for an ARTn-MTP process. The 1000-atom ARTn-SW a-Si configuration (1000-aSi-SW initial) was refined through ARTn-MTP, resulting in the (1000-aSi-SW final) configuration. The goal was to assess the ARTn-MTP process's ability to refine configurations optimized with a semi-empirical potential. The energy dropped by  $-23.25 \text{ meV/atom}$ , and structural properties, shown in Fig. 9 and summarized in Tab. III, reveal significant improvements. The number of dangling and floating bonds decreased, reducing total defects by 3%. Bond angles (Fig. 9 b) are closer to the ideal  $109.5^\circ$ , with a narrower spread in the final model. Bond lengths were concentrated around  $2.38 \text{ \AA}$ , aligning with experimental values, and the radial distribution function in Fig. 9 c confirmed this. The 1000-aSi-SW final and 100k-GAP18 models showed better agreement with experimental data than the initial configuration. The structure factor, in Fig. 9 d, also matched experimental  $S(q)$ . The excess

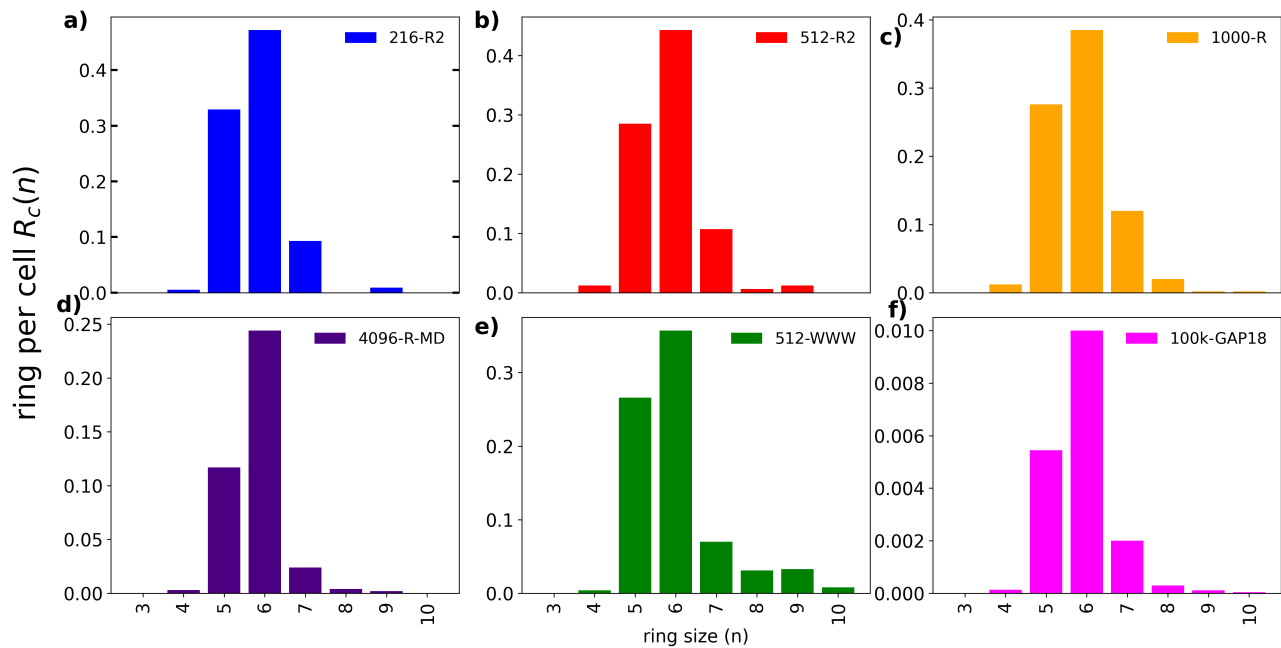


**Fig. 8** Ring statistics for ARTn-MTP generated models as well as those derived from the 512-WWW model and 100k-GAP18 atom models.

Properties	1000-aSi-SW initial	1000-aSi-SW final
Density ( $\text{g}/\text{cm}^3$ )	2.20	2.24
Fourfold Si (%)	94.60	97.60
Threefold Si (%)	3.00	0.90
Fivefold Si (%)	2.40	1.50
Average bond length ( $\sigma$ )	2.38 (0.05)	2.38 (0.03)
Average bond angle ( $\sigma$ )	109.11 (10.91)	109.12 (11.26)
Average coordination number	3.99	4.01
$\Delta E$ (eV / atom)	0.20	0.18
Bulk modulus (GPa)	65.86	68.87
Crystallinity (%)	0.00	0.00

**Tab. III** Structural and elastic properties for 1000-aSi-SW initial and 1000-aSi-SW final configurations: coordination defects, coordination number, average bond length, average bond angle, bulk modulus and energy difference per atom between amorphous state and crystalline Si. Standard deviations are provided in parentheses. The ART-SW optimized configurations (1000-aSi-SW initial) served as the input for the ARTn-MTP refined configurations (1000-aSi-SW final).

energy ( $\Delta E$ ) decreased from 0.2021 eV/atom (initial) to 0.1789 eV/atom (final), falling within the experimental range of 0.135 – 0.205 eV/atom<sup>81</sup>. The final configuration, with lower excess energy, is more stable and realistic. The bulk modulus increased from 65.8573 GPa (initial) to 68.8690 GPa (final), indicating enhanced stiffness. These results demonstrate that the ARTn-MTP coupling scheme effectively relaxes a semi-empirically optimized amorphous configuration.

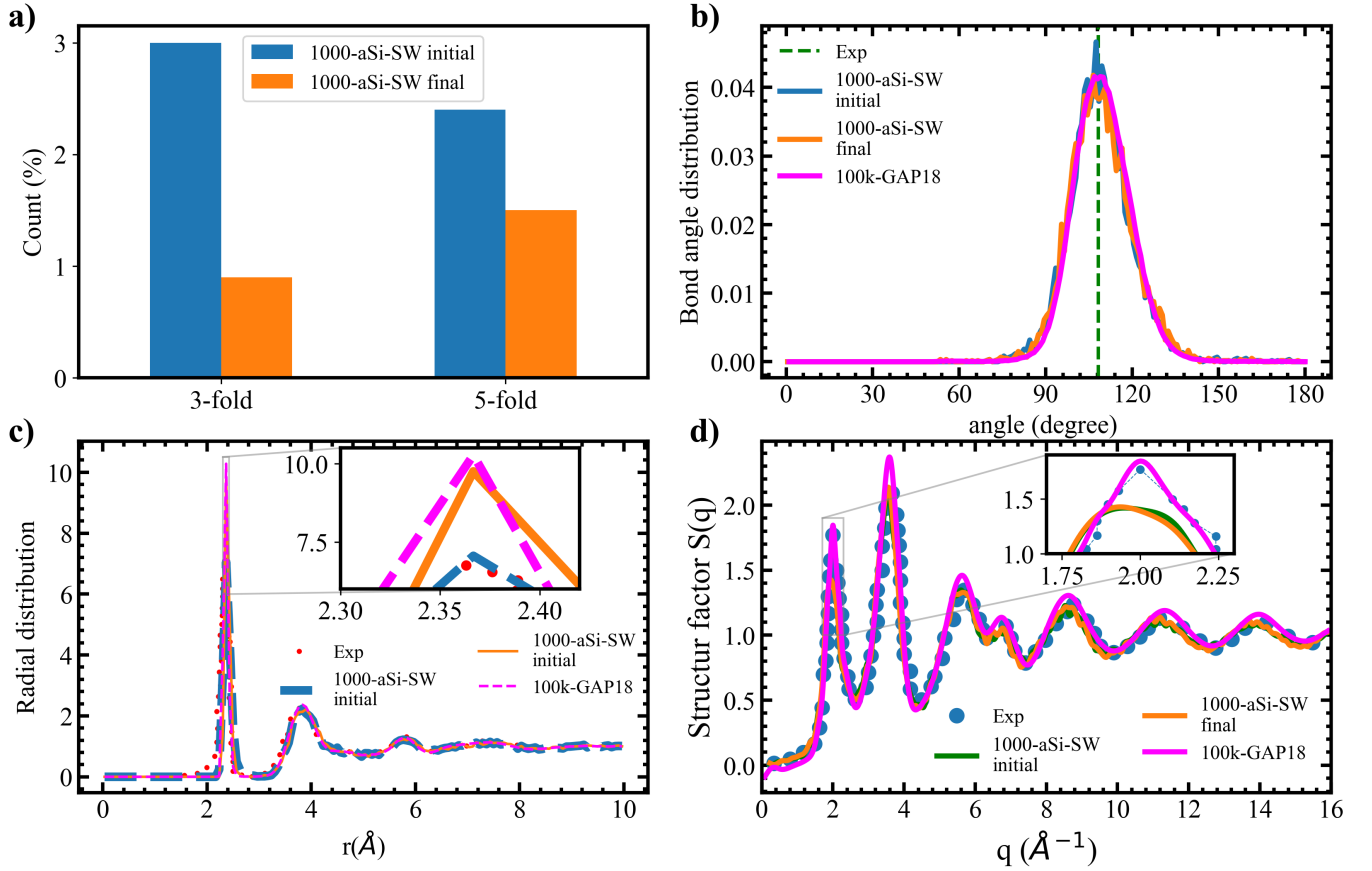
#### D. Stiffness

We calculated the bulk modulus  $B$  of our models and of the models found in the literature. The results are presented in Fig. 10. We include the bulk modulus value obtained from density functional theory (DFT) simulations reported in Ref.<sup>82</sup>, which is 82.5 GPa. For our 216-R2 configuration with 100% 4-fold coordination, we obtained a bulk modulus of 80.01 GPa. The 512-R2 model yields a bulk modulus of 77.53 GPa, closely matching the 512-WWW model’s value of 77.41 GPa. In contrast, other models such as 512-MD, 512-INV, and 512-RMC exhibit lower bulk modulus values of 71.18 GPa, 69.00 GPa, and 70.90 GPa, respectively. The 1000-R model demonstrates a bulk modulus of 76.46 GPa. Our largest models, the 4096-R-MD and 100k-GAP18, yield bulk modulus values of 77.93 GPa and 79.56 GPa, respectively. All of these values were obtained using our unified machine learning potential developed for the Si, O, and SiO<sub>2</sub> systems. Other potentials may yield different results. To our knowledge, there are no clear experimental benchmark values for the bulk modulus of amorphous silicon.

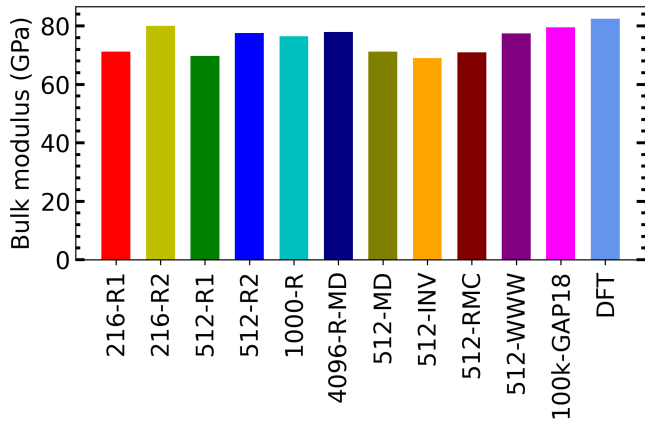
#### E. Potential energy

Fig. 11 shows the relationship between energy decrease and the number of events for the model 216-R2. As can be seen, the energy decreases as the number of events increase. A detailed analysis of the events and key parameters is provided in the Nature of the Relaxation section. The experimental excess energy interval is indicated by the light red shaded region in the figure for reference. The inset of Fig. 11 shows the excess energy per atom for each





**Fig. 9** Local structural properties of ARTn-MTP refined configurations (1000-aSi-SW final) compared to ART-SW optimized configurations (1000-aSi-SW initial). a) Initial and final counts of 3-fold and 5-fold defects, b) bond angle distribution function, c) radial distribution function, and d) structure factor. For figures (b), (c), and (d), experimental data and results from the 100k-GAP-18 atom model are included to assess the quality of both the initial and final configurations of the 1000-aSi-SW model. The ART-SW optimized configurations served as the input for the ARTn-MTP refined configurations.



**Fig. 10** Bulk modulus for ARTn-MTP generated models as well as models from the literature.

of our models. These values are also presented in table IV. All models fall within the experimental excess energy interval<sup>81</sup>, as detailed in the inset. Notably, the 216-R2

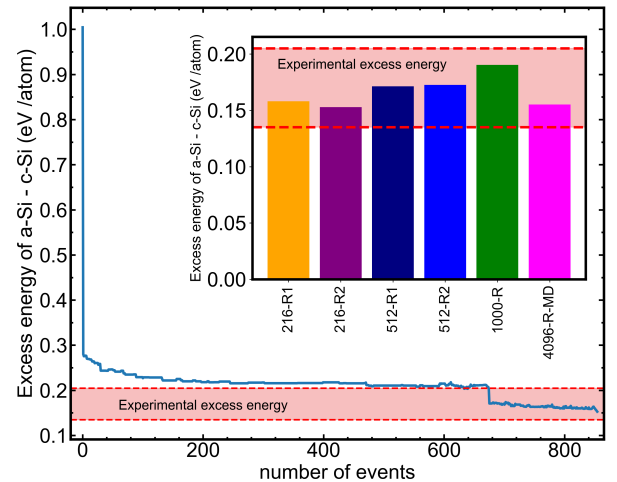


**Fig. 11** Excess energy between ART-MTP configurations (a-Si) and crystalline silicon (c-Si) as a function of the number of accepted events. A total of 4 events per atom was required to achieve 100% 4-fold coordination in 216-R2 a-Si model.

Models	$\rho_i$ (g/cm <sup>3</sup> )	$\Delta E$ (eV / atom)	$\rho_f$ (g/cm <sup>3</sup> )
216-R1	2.23	0.16	2.24 (2.23)
216-R2	2.28	0.15	2.25 (2.24)
512-R1	2.23	0.17	2.23 (2.22)
512-R2	2.28	0.17	2.25 (2.24)
1000-R	2.28	0.19	2.25 (2.24)
4096-R-MD	2.28	0.16	2.26 (2.25)
Exp	2.2800 <sup>83</sup>	0.135 – 0.205 <sup>81</sup>	-

**Tab. IV** Initial ( $\rho_i$ ) and final ( $\rho_f$ ) density for the ARTn-MTP generated a-Si model. Each model was randomly filled and the simulation box sizes was adjusted to match the initial density, which was maintained from the beginning to the end of the ARTn simulation. The final density was obtained by relaxing each of the generated models to 0.5 K as described in main test. The values in parentheses were obtained by relaxing each model at 300 K and 1 atm. The excess energy in eV per atom ( $\Delta E$ ) relative to crystalline silicon is presented alongside the experimental excess energy.

model, which initially contained over 70% coordination defects (see Fig. 2), was efficiently relaxed to achieve 100% 4-fold coordination and the lowest excess energy of 0.17 eV/atom with just 4 events per atom. To our knowledge, with the exception of a few Keating-potential-based WWW models<sup>10,23,78</sup>, no other method, including DFT<sup>84</sup>, has yielded a model of a-Si with no coordination defects.

#### F. Density

We computed the density of our models at 0 K. The final density was obtained by running a 50 ps molecular dynamics simulation, cooling the system from 300 K to 0.5 K, and then holding it at 0.5 K for an additional 50 ps, while barostatting the system at 0 Pa. In separate simulations, we also equilibrated each of the aforementioned models at 300 K and 1 atm for 100 ps. The results are presented in table IV. The ART-MTP a-Si density values at 0 K are 0.71% to 1.94% larger than the experimental density measured at room temperature. ART-MTP a-Si density at 300 K and 1 atm is characterized by density values 1.18% to 2.43% larger than experimental densities. The MTP potential is trained using a generalized gradient approximation exchange-correlation functional, which is known to overestimate the density of crystalline silicon by 2 %<sup>85</sup>. Retraining the MTP on a higher-accuracy exchange-correlation functional, such as the restored regularized strongly constrained and appropriately normed meta-generalized gradient approximation<sup>86</sup> is likely to solve this small discrepancy with experimental values.

#### G. Nature of the relaxation

The primary goal is not only to generate high-quality amorphous structures but also to understand the underlying physics of the relaxation process in amorphous systems over time. Thus, to understand the relaxation process in our amorphous system, we analyze simulation data, focusing on key parameters such as barrier distribution,

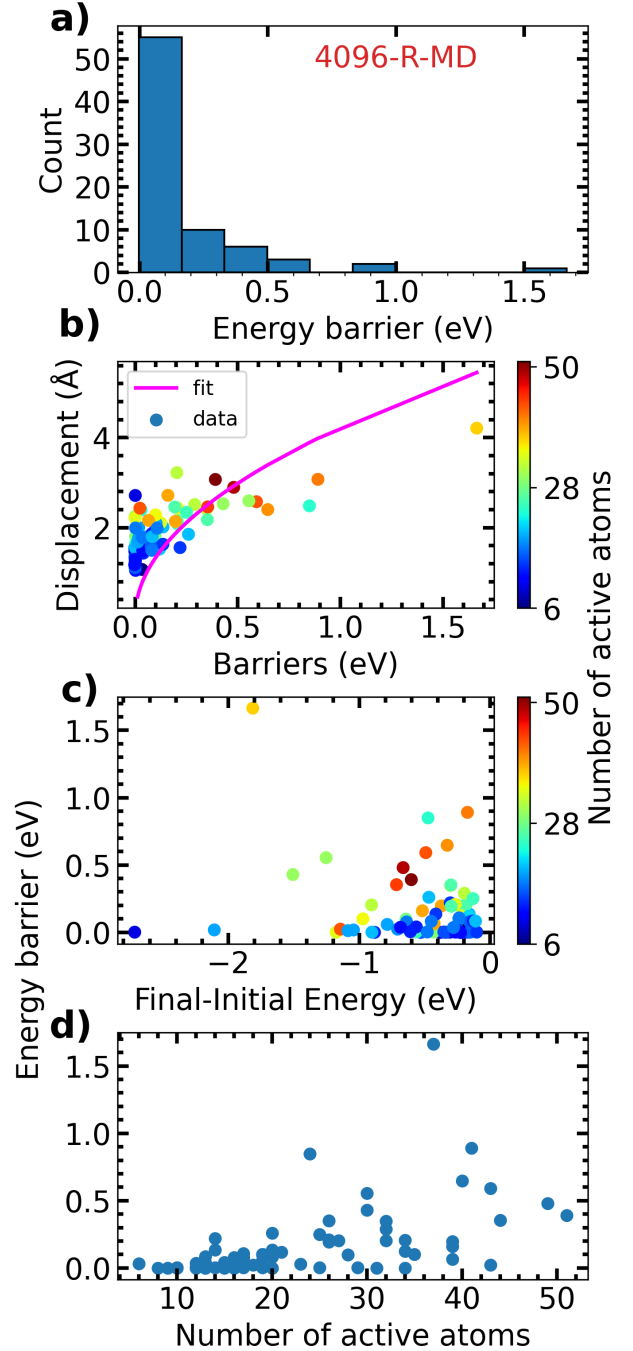


**Fig. 12** Analysis of accepted Events in ARTn-MTP optimization: a) Barrier distribution, b) square root of squared atomic displacement versus energy barrier, c) energy barrier as a function of energy decrease, and d) energy barrier versus active atoms during events

atomic displacements, active atoms, and energy decrease, considering only accepted events as detailed in Fig. 12. These parameters can help provide insights into the nature and mechanism of the relaxation process. The data were collected under normal deformation, excluding shear deformation during the simulation. We first examine the

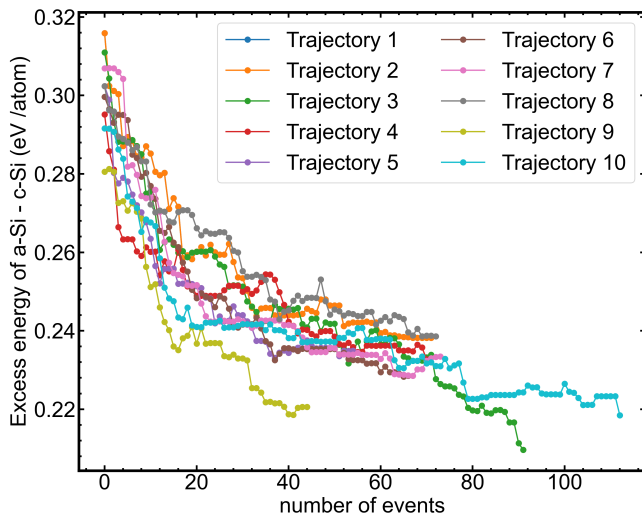


**Fig. 13** Nonlinear optimization effects characterized by excess energy per atom and number of events computed from independent runs with identical input Configuration

correlation between atomic displacement and energy barriers. A clear correlation is observed: larger displacements are typically associated with higher energy barriers and more active atoms, as shown in Fig. 12 (a). To further validate this, we calculate the correlation between the square of the atomic displacement and the energy barriers. According to Hooke’s law, we expect a quadratic relationship between energy and displacement. When we plot energy against the square of the displacement, we expect a linear relationship, which our results confirm, yielding a strong correlation. Next, we find no significant correlation between the energy barriers and the energy gain, nor between energy gain and the number of active atoms, which is consistent with previous studies<sup>87</sup>. Furthermore, no correlation exists between the number of atoms displaced up to the saddle point and the final state. As illustrated in Fig. 12(d), a correlation exists between energy barriers and the number of active atoms, with higher energy barriers typically involving a greater number of active atoms. On average, the number of active atoms varies from 10 to 30, with a mean of around 20 atoms that moves by more than 0.1 Å per event. This suggests that each event is localized, typically involving a cutoff radius of less than 7 Å. The microstructural changes primarily occur within a few neighboring cells, indicating a localized relaxation process. The relationship between the aforementioned parameters and the number of randomly displaced atoms at the start of ARTn searches (which depends on the cutoff and the central atom) was not investigated in this work.

#### H. Computational cost and nonlinear optimization process

One of the primary challenges in computational materials modeling is finding the right balance between accuracy

and computational cost. In this work, we present the first-ever coupling between ARTn and machine learning potentials, and we document the computational cost involved in preparing our amorphous system.

For the system of 216 atoms, the optimization of configurations required 0.0615 core-years and involved 55.20 millions force evaluations. Notably, one of the 216 atoms was optimized to achieve 100% 4-fold coordination. For the larger systems, the computational costs were as follows: the 512-atom system took 0.22 core-years, and the 1000-atom system required 0.34 core-years. Finally, for the 4096-atom system, we recorded 0.09 core-years to refine the MD configuration, with 37.25 million force evaluations. As mentioned in previous sections, this configuration achieved 98.05% 4-fold coordination and an excess energy of 0.15 eV per atom, which is closer to the experimentally observed low excess energy value.

The nonlinear optimization process within the ARTn framework was explored using a randomly generated 216-atom input configuration, with independent runs conducted using the same number of steps. Data were collected from these independent trajectories. Fig. 13 illustrates the relationship between excess energy levels and the number of accepted events for each trajectory. The results reveal varying numbers of accepted events and relaxation levels across the trajectories. Among the independent runs, the lowest number of accepted events was 45, while the highest was 113. Despite this difference, both systems achieved nearly identical excess energy levels. The mean number of accepted events was approximately 75, with most systems exhibiting higher excess energy than the system with 92 accepted events, which showed the lowest excess energy. These findings are indicative of a nonlinear optimization process.

#### IV. Conclusions

In this paper, we investigated a-Si using ARTn coupled with a MTP. Seven models of varying sizes were constructed. They displayed excellent agreement with both experimental data and data obtained using a state-of-the-art 100,000-atom MD-based model leveraging a different MLIP. The proposed ARTn-MTP optimizer can further refine and relax configurations that have already been previously optimized using ARTn with a semi-empirical model. Additionally, the relaxation level of a-Si generated through standard molecular dynamics simulations via the melt-quench process can also be improved using the ARTn-MTP coupling scheme. We have generated high-quality amorphous structures of various sizes, including 216, 512, and 1000 atoms, without any traces of local crystallinity. We also found that starting the ARTn simulation with a randomly filled configuration results in an optimized structure with less crystallinity compared to initiating the simulation with an MD pre-relaxed configuration. The question of local crystallinity, its link with defects and the ideal amorphous structure has not been addressed previously, due to the lack of good quality models gen-

erated through different pathways (non-dynamic, such as with ARTn, and melt-and-quench, for example). The results presented here raise numerous related research questions that could further enhance our understanding of a-Si and its fabrication. Future research could focus on increasing system sizes while minimizing coordination and ring defects, for example, by targeting over-coordinated, under-coordinated, and high-energy atoms during event searches. Further studies will investigate the origins of crystallinity, explore its formation during the preparation of amorphous silicon, and examine methods for producing large-scale amorphous a-Si free of crystallinity.

It is now clear that ARTn coupled with MLIPs is a very effective approach to model a-Si. However, if the primary goal is to replicate experimental conditions as

accurately as possible, further innovation is necessary. Experimentally, a-Si is produced mainly by chemical vapor deposition and ion implantation; representative elementary volumes range from scales of tens of nanometers to micrometers, and processing times on the order of seconds to hours. Accessing such time- and length-scales would enable both applied studies—e.g. device-scale simulations—and fundamental studies—e.g. assessing the degree of hyperuniformity of a-Si. Although modeling large systems is straightforward thanks to parallel computing, reaching long timescales remains an elusive challenge. While there are examples of ARTn-based techniques reaching such timescales in irradiated c-Si and a-Si<sup>88–92</sup>, further development is necessary in order for these methods to routinely achieve such outcome.

- 
- [1] Robert Street. *Technology and applications of amorphous silicon*, volume 37. Springer Science & Business Media, 1999.
- [2] David E Carlson and Cristopher R Wronski. Amorphous silicon solar cell. *Applied Physics Letters*, 28(11):671–673, 1976.
- [3] Martin J Powell. The physics of amorphous-silicon thin-film transistors. *IEEE transactions on Electron Devices*, 36(12):2753–2763, 1989.
- [4] Li-Feng Cui, Riccardo Ruffo, Candace K Chan, Hailin Peng, and Yi Cui. Crystalline-amorphous core-shell silicon nanowires for high capacity and high current battery electrodes. *Nano letters*, 9(1):491–495, 2009.
- [5] Baris Key, Rangeet Bhattacharyya, Mathieu Morcrette, Vincent Seznec, Jean-Marie Tarascon, and Clare P Grey. Real-time nmr investigations of structural changes in silicon electrodes for lithium-ion batteries. *Journal of the American Chemical Society*, 131(26):9239–9249, 2009.
- [6] Ross Birney, J Steinlechner, Z Tornasi, Sean MacFoy, David Vine, AS Bell, Desmond Gibson, Jim Hough, Sheila Rowan, P Sortais, et al. Amorphous silicon with extremely low absorption: Beating thermal noise in gravitational astronomy. *Physical review letters*, 121(19):191101, 2018.
- [7] Laurent J Lewis. Fifty years of amorphous silicon models: the end of the story? *Journal of Non-Crystalline Solids*, 580:121383, 2022.
- [8] Ata Madanchi, Emna Azek, Karim Zongo, Laurent K Béland, Normand Mousseau, and Lena Simine. Is the future of materials amorphous? challenges and opportunities in simulations of amorphous materials. *arXiv preprint arXiv:2410.05035*, 2024.
- [9] William Houlder Zachariasen. The atomic arrangement in glass. *Journal of the American Chemical Society*, 54(10):3841–3851, 1932.
- [10] F Wooten, K Winer, and D Weaire. Computer generation of structural models of amorphous si and ge. *Physical review letters*, 54(13):1392, 1985.
- [11] RLC Vink, GT Barkema, MA Stijnman, and RH Bisseling. Device-size atomistic models of amorphous silicon. *Physical Review B*, 64(24):245214, 2001.
- [12] S Roorda, WC Sinke, JM Poate, DC Jacobson, S Dierker, BS Dennis, DJ Eaglesham, F Spaepen, and P Fuoss. Structural relaxation and defect annihilation in pure amorphous silicon. *Physical review B*, 44(8):3702, 1991.
- [13] Khalid Laaziri, S Kycia, S Roorda, M Chicoine, JL Robertson, J Wang, and SC Moss. High resolution radial distribution function of pure amorphous silicon. *Physical review letters*, 82(17):3460, 1999.
- [14] Khalid Laaziri, S Kycia, S Roorda, M Chicoine, JL Robertson, J Wang, and SC Moss. High-energy x-ray diffraction study of pure amorphous silicon. *Physical Review B*, 60(19):13520, 1999.
- [15] Carl Lévesque, Sjoerd Roorda, François Schiettekatte, and Normand Mousseau. Internal mechanical dissipation mechanisms in amorphous silicon. *Physical Review Materials*, 6(12):123604, 2022.
- [16] E Holmström, Bianca Haberl, Olli H Pakarinen, Kai Nordlund, Flyura Djurabekova, Raul Arenal, James S Williams, Jodie E Bradby, Timothy C Petersen, and ACY Liu. Dependence of short and intermediate-range order on preparation in experimental and modeled pure a-si. *Journal of Non-Crystalline Solids*, 438:26–36, 2016.
- [17] F Kail, J Farjas, P Roura, C Secouard, O Nos, J Bertomeu, and P Roca i Cabarrocas. The configurational energy gap between amorphous and crystalline silicon. *physica status solidi (RRL)—Rapid Research Letters*, 5(10-11):361–363, 2011.
- [18] S Roorda, S Doorn, WC Sinke, PMLO Scholte, and E Van Loenen. Calorimetric evidence for structural relaxation in amorphous silicon. *Physical review letters*, 62(16):1880, 1989.
- [19] GN Van den Hoven, ZN Liang, L Niesen, and JS Custer. Evidence for vacancies in amorphous silicon. *Physical review letters*, 68(25):3714, 1992.
- [20] J Fortner and JS Lannin. Radial distribution functions of amorphous silicon. *Physical Review B*, 39(8):5527, 1989.
- [21] Bianca Haberl, Amelia Chi Ying Liu, Jodie E Bradby, Simon Ruffell, Jim S Williams, and Paul Munroe. Structural characterization of pressure-induced amorphous silicon. *Physical Review B—Condensed Matter and Materials Physics*, 79(15):155209, 2009.
- [22] GT Barkema and Normand Mousseau. Event-based relaxation of continuous disordered systems. *Physical review letters*, 77(21):4358, 1996.
- [23] Gerard T Barkema and Normand Mousseau. High-quality continuous random networks. *Physical Review*

- B*, 62(8):4985, 2000.
- [24] Volker L Deringer, Noam Bernstein, Albert P Bartók, Matthew J Cliffe, Rachel N Kerber, Lauren E Marbella, Clare P Grey, Stephen R Elliott, and Gábor Csányi. Realistic atomistic structure of amorphous silicon from machine-learning-driven molecular dynamics. *The journal of physical chemistry letters*, 9(11):2879–2885, 2018.
- [25] Joao F Justo, Martin Z Bazant, Efthimios Kaxiras, Vasily V Bulatov, and Sidney Yip. Interatomic potential for silicon defects and disordered phases. *Physical review B*, 58(5):2539, 1998.
- [26] Manabu Ishimaru, Shinji Munetoh, and Teruaki Motooka. Generation of amorphous silicon structures by rapid quenching: A molecular-dynamics study. *Physical Review B*, 56(23):15133, 1997.
- [27] AC Wright and MF Thorpe. Eighty years of random networks. *physica status solidi (b)*, 250(5):931–936, 2013.
- [28] David S Sholl and Janice A Steckel. *Density functional theory: a practical introduction*. John Wiley & Sons, 2022.
- [29] Iam Torrens. *Interatomic potentials*. Elsevier, 2012.
- [30] RL McGreevy and L Pusztai. Reverse monte carlo simulation: a new technique for the determination of disordered structures. *Molecular simulation*, 1(6):359–367, 1988.
- [31] RL McGreevy and MA Howe. Rmc: modeling disordered structures. *Annual Review of Materials Science*, 22(1):217–242, 1992.
- [32] O Gereben, P Jóvári, L Temleitner, and L Pusztai. A new version of the rmc++ reverse monte carlo programme, aimed at investigating the structure of covalent glasses. *Journal of Optoelectronics and Advanced Materials*, 9(10):3021, 2007.
- [33] SJ Gurman and RL McGreevy. Reverse monte carlo simulation for the analysis of exafs data. *Journal of Physics: Condensed Matter*, 2(48):9463, 1990.
- [34] Robert L McGreevy. Reverse monte carlo modelling. *Journal of Physics: Condensed Matter*, 13(46):R877, 2001.
- [35] A Pandey, Parthapratim Biswas, and DA Drabold. Force-enhanced atomic refinement: Structural modeling with interatomic forces in a reverse monte carlo approach applied to amorphous si and sio 2. *Physical Review B*, 92(15):155205, 2015.
- [36] Dale Igram, Bishal Bhattarai, Parthapratim Biswas, and David A Drabold. Large and realistic models of amorphous silicon. *Journal of Non-Crystalline Solids*, 492:27–32, 2018.
- [37] Parthapratim Biswas, Raymond Atta-Fynn, David Drabold, et al. The inclusion of experimental information in first principles modelling of materials. *Journal of Physics: Condensed Matter*, 16(44):S5173, 2004.
- [38] Rachid Malek and Normand Mousseau. Dynamics of lennard-jones clusters: A characterization of the activation-relaxation technique. *Physical Review E*, 62(6):7723, 2000.
- [39] Normand Mousseau, Laurent Karim Béland, Peter Brommer, Jean-François Joly, Fedwa El-Mellouhi, Eduardo Machado-Charry, Mihai-Cosmin Marinica, and Pascal Pochet. The activation-relaxation technique: Art nouveau and kinetic art. *Journal of Atomic and Molecular Physics*, 2012, 2012.
- [40] Antoine Jay, Miha Gunde, Nicolas Salles, Matic Poberžnik, Layla Martin-Samos, Nicolas Richard, Stefano de Gironcoli, Normand Mousseau, and Anne Hémerlyck. Activation-relaxation technique: An efficient way to find minima and saddle points of potential energy surfaces. *Computational Materials Science*, 209:111363, 2022.
- [41] Normand Mousseau and Gerard T Barkema. Exploring high-dimensional energy landscapes. *Computing in Science & Engineering*, 1(2):74–80, 1999.
- [42] Patrick Ganster, Laurent Karim Béland, and Normand Mousseau. First stages of silicon oxidation with the activation relaxation technique. *Physical Review B*, 86(7):075408, 2012.
- [43] F El-Mellouhi and Normand Mousseau. Ab initio characterization of arsenic vacancy diffusion pathways in gaas with siest-a-rt. *Applied Physics A*, 86:309–312, 2007.
- [44] Nicolas Salles, Nicolas Richard, Normand Mousseau, and Anne Hémerlyck. Strain-driven diffusion process during silicon oxidation investigated by coupling density functional theory and activation relaxation technique. *The Journal of Chemical Physics*, 147(5):054701, 2017.
- [45] Jean-François Joly, Laurent Karim Béland, Peter Brommer, Fedwa El-Mellouhi, and Normand Mousseau. Optimization of the kinetic activation-relaxation technique, an off-lattice and self-learning kinetic monte-carlo method. In *Journal of Physics: Conference Series*, volume 341, page 012007. IOP Publishing, 2012.
- [46] Hao Sun and Laurent Karim Béland. Statistical distribution of spontaneous recombination radii of frenkel pairs in fcc and bcc metals. *Acta Materialia*, 229:117814, 2022.
- [47] Hao Sun and Laurent Karim Béland. Calculation of the recombination radii between various point defects and defect clusters in nickel via kinetic activation relaxation technique. *Journal of Nuclear Materials*, 586:154663, 2023.
- [48] Mickaël Trochet, Normand Mousseau, Laurent Karim Béland, and Graeme Henkelman. Off-lattice kinetic monte carlo methods. *Handbook of materials modeling: Methods: Theory and modeling*, pages 715–743, 2020.
- [49] Laurent Karim Béland, Peter Brommer, Fedwa El-Mellouhi, Jean-François Joly, and Normand Mousseau. Kinetic activation-relaxation technique. *Physical Review E—Statistical, Nonlinear, and Soft Matter Physics*, 84(4):046704, 2011.
- [50] Jörg Behler and Michele Parrinello. Generalized neural-network representation of high-dimensional potential-energy surfaces. *Physical review letters*, 98(14):146401, 2007.
- [51] Volker L Deringer, Miguel A Caro, and Gábor Csányi. Machine learning interatomic potentials as emerging tools for materials science. *Advanced Materials*, 31(46):1902765, 2019.
- [52] Guanjie Wang, Changrui Wang, Xuanguang Zhang, Zefeng Li, Jian Zhou, and Zhimei Sun. Machine learning interatomic potential: Bridge the gap between small-scale models and realistic device-scale simulations. *Iscience*, 27(5), 2024.
- [53] Alireza Khorshidi and Andrew A Peterson. Amp: A modular approach to machine learning in atomistic simulations. *Computer Physics Communications*, 207:310–324, 2016.
- [54] A. P. Bartok. *The Gaussian Approximation Potential: an interatomic potential derived from first principles quantum mechanics*. Springer Science & Business Media, 2010.
- [55] Albert P Bartók, James Kermode, Noam Bernstein, and Gábor Csányi. Machine learning a general-purpose interatomic potential for silicon. *Physical Review X*, 8(4):041048, 2018.
- [56] Aidan P Thompson, Laura P Swiler, Christian R Trott,

- Stephen M Foiles, and Garritt J Tucker. Spectral neighbor analysis method for automated generation of quantum-accurate interatomic potentials. *Journal of Computational Physics*, 285:316–330, 2015.
- [57] Alexander V Shapeev. Moment tensor potentials: A class of systematically improvable interatomic potentials. *Multiscale Modeling & Simulation*, 14(3):1153–1173, 2016.
- [58] Ruiyang Li, Eungkyu Lee, and Tengfei Luo. A unified deep neural network potential capable of predicting thermal conductivity of silicon in different phases. *Materials Today Physics*, 12:100181, 2020.
- [59] Zheyong Fan, Zezhu Zeng, Cunzhi Zhang, Yanzhou Wang, Keke Song, Haikuan Dong, Yue Chen, and Tapio Ala-Nissila. Neuroevolution machine learning potentials: Combining high accuracy and low cost in atomistic simulations and application to heat transport. *Physical Review B*, 104(10):104309, 2021.
- [60] Wenwen Li and Yasunobu Ando. Dependence of a cooling rate on structural and vibrational properties of amorphous silicon: A neural network potential-based molecular dynamics study. *The Journal of Chemical Physics*, 151(11), 2019.
- [61] Volker L Deringer, Noam Bernstein, Gábor Csányi, Chihab Ben Mahmoud, Michele Ceriotti, Mark Wilson, David A Drabold, and Stephen R Elliott. Origins of structural and electronic transitions in disordered silicon. *Nature*, 589(7840):59–64, 2021.
- [62] Karim Zongo, Hao Sun, Claudiane Ouellet-Plamondon, and Laurent Karim Béland. A unified moment tensor potential for silicon, oxygen, and silica. *npj Computational Materials*, 10(1):218, 2024.
- [63] Kokou Gawonou N’Tsouaglo. Caratérisation de la surface d’énergie potentielle des matériaux complexes et son application sur la cinétique du sio<sub>2</sub>/si. 2015.
- [64] Antoine Jay, Christophe Huet, Nicolas Salles, Miha Gunde, Layla Martin-Samos, Nicolas Richard, Georges Landa, Vincent Goiffon, Stefano de Gironcoli, Anne Hemeryck, and Normand Mousseau. Finding reaction pathways and transition states: R-ARTn and d-ARTn as an efficient and versatile alternative to string approaches. *Journal of Chemical Theory and Computation*, 16(10):6726–6734, 2020.
- [65] M. Gunde, A. Jay, M. Poberžnik, N. Salles, N. Richard, G. Landa, Normand Mousseau, L. Martin-Samos, and A. Hemeryck. Exploring potential energy surfaces to reach saddle points above convex regions. *The Journal of Chemical Physics*, 160(23):232501, June 2024.
- [66] Normand Mousseau and GT Barkema. Traveling through potential energy landscapes of disordered materials: The activation-relaxation technique. *Physical Review E*, 57(2):2419, 1998.
- [67] Simen NH Eliassen, Jesper Friis, Inga G Ringdalen, Normand Mousseau, Mickaël Trochet, and Yanjun Li. Atomistic approach to simulate kink migration and kink-pair formation in silicon: The kinetic activation-relaxation technique. *Physical Review B*, 100(15):155305, 2019.
- [68] Eduardo Machado-Charry, Laurent Karim Béland, Damien Caliste, Luigi Genovese, Thierry Deutsch, Normand Mousseau, and Pascal Pochet. Optimized energy landscape exploration using the ab initio based activation-relaxation technique. *The Journal of chemical physics*, 135(3), 2011.
- [69] Laurent Karim Béland, Eduardo Machado-Charry, Pascal Pochet, and Normand Mousseau. Strain effects and intermixing at the si surface: Importance of long-range elastic corrections in first-principles calculations. *Physical Review B*, 90(15):155302, 2014.
- [70] K Zongo, LK Béland, and C Ouellet-Plamondon. First-principles database for fitting a machine-learning silicon interatomic force field. *MRS Advances*, 7(2-3):39–47, 2022.
- [71] Ivan S Novikov, Konstantin Gubaev, Evgeny V Podryabinkin, and Alexander V Shapeev. The mlip package: moment tensor potentials with mpi and active learning. *Machine Learning: Science and Technology*, 2(2):025002, 2020.
- [72] Matthew J Cliffe, Albert P Bartók, Rachel N Kerber, Clare P Grey, Gábor Csányi, and Andrew L Goodwin. Structural simplicity as a restraint on the structure of amorphous silicon. *Physical Review B*, 95(22):224108, 2017.
- [73] Alexander Stukowski. Visualization and analysis of atomistic simulation data with ovito—the open visualization tool. *Modelling and Simulation in Materials Science and Engineering*, 18(1):015012, 2009.
- [74] Sébastien Le Roux and Philippe Jund. Ring statistics analysis of topological networks: New approach and application to amorphous ges<sub>2</sub> and sio<sub>2</sub> systems. *Computational Materials Science*, 49(1):70–83, 2010.
- [75] Sébastien Le Roux and Valeri Petkov. Isaacs–interactive structure analysis of amorphous and crystalline systems. *Journal of Applied Crystallography*, 43(1):181–185, 2010.
- [76] Aidan P Thompson, H Metin Aktulga, Richard Berger, Dan S Bolintineanu, W Michael Brown, Paul S Crozier, Pieter J in’t Veld, Axel Kohlmeyer, Stan G Moore, Trung Dac Nguyen, et al. Lammmps—a flexible simulation tool for particle-based materials modeling at the atomic, meso, and continuum scales. *Computer Physics Communications*, 271:108171, 2022.
- [77] E. Maras, O. Trushin, A. Stukowski, T. Ala-Nissila, and H. Jónsson. Global transition path search for dislocation formation in Ge on Si(001). *Computer Physics Communications*, 205:13–21, August 2016.
- [78] Anup Pandey, Parthapratim Biswas, and David A Drabold. Inversion of diffraction data for amorphous materials. *Scientific Reports*, 6(1):33731, 2016.
- [79] Frank H Stillinger and Thomas A Weber. Computer simulation of local order in condensed phases of silicon. *Physical review B*, 31(8):5262, 1985.
- [80] RLC Vink, GT Barkema, WF Van der Weg, and Normand Mousseau. Fitting the stillinger–weber potential to amorphous silicon. *Journal of non-crystalline solids*, 282(2-3):248–255, 2001.
- [81] Dil K Limbu, Raymond Atta-Fynn, David A Drabold, Stephen R Elliott, and Parthapratim Biswas. Information-driven inverse approach to disordered solids: Applications to amorphous silicon. *Physical Review Materials*, 2(11):115602, 2018.
- [82] Murat Durandurdu and DA Drabold. Ab initio simulation of first-order amorphous-to-amorphous phase transition of silicon. *Physical Review B*, 64(1):014101, 2001.
- [83] J S Custer, Michael O Thompson, DC Jacobson, JM Poate, S Roorda, WC Sinke, and F Spaepen. Density of amorphous si. *Applied physics letters*, 64(4):437–439, 1994.
- [84] Andreas Pedersen, Laurent Pizzagalli, and Hannes Jónsson. Optimal atomic structure of amorphous silicon obtained from density functional theory calculations. *New Journal of Physics*, 19(6):063018, 2017.

- [85] Ankit Jain and Alan JH McGaughey. Effect of exchange–correlation on first-principles-driven lattice thermal conductivity predictions of crystalline silicon. *Computational Materials Science*, 110:115–120, 2015.
- [86] James W Furness, Aaron D Kaplan, Jinliang Ning, John P Perdew, and Jianwei Sun. Accurate and numerically efficient r2scan meta-generalized gradient approximation. *The journal of physical chemistry letters*, 11(19):8208–8215, 2020.
- [87] Housseem Kallel, Normand Mousseau, and François Schiettekatte. Evolution of the potential-energy surface of amorphous silicon. *Physical Review Letters*, 105(4):045503, 2010.
- [88] Laurent Karim Béland, Yonathan Anahory, Dries Smeets, Matthieu Guihard, Peter Brommer, Jean-François Joly, Jean-Christophe Pothier, Laurent J Lewis, Normand Mousseau, and François Schiettekatte. Replenish and relax: Explaining logarithmic annealing in ion-implanted c-si. *Physical review letters*, 111(10):105502, 2013.
- [89] Laurent Karim Béland and Normand Mousseau. Long-time relaxation of ion-bombarded silicon studied with the kinetic activation-relaxation technique: Microscopic description of slow aging in a disordered system. *Physical Review B*, 88(21):214201, 2013.
- [90] Jean-Francois Joly, Laurent Karim Béland, Peter Brommer, and Normand Mousseau. Contribution of vacancies to relaxation in amorphous materials: A kinetic activation-relaxation technique study. *Physical Review B—Condensed Matter and Materials Physics*, 87(14):144204, 2013.
- [91] Gawonou Kokou N’Tsouaglo, Laurent Karim Béland, Jean-François Joly, Peter Brommer, Normand Mousseau, and Pascal Pochet. Probing potential energy surface exploration strategies for complex systems. *Journal of Chemical Theory and Computation*, 11(4):1970–1977, 2015.
- [92] Laurent Karim Béland, Yuri N Osetsky, Roger E Stoller, and Haixuan Xu. Slow relaxation of cascade-induced defects in fe. *Physical Review B*, 91(5):054108, 2015.

### Acknowledgements

We thank the Digital Research Alliance of Canada for generous allocation of compute resources. Financial support was provided by the Natural Sciences and Engineering Research Council of Canada (NSERC) and the Association canadienne-française pour l’avancement des sciences (ACFAS), and the Canada Research Chair on Sustainable Multifunctional Construction Materials.

### Author contributions

L.K.B. initiated and coordinated the research project. K.Z. performed all ARTn-MTP and molecular dynamics simulations, as well as the analyses presented in this work. All authors—K.Z., H.S., N.M., L.K.B., and C.O.P.—contributed to the writing of the paper. C.O.P., N.M., and L.K.B. supervised K.Z., while C.O.P. and L.K.B. provided the necessary computing resources.

### Competing interests

The authors declare no conflict of interest.